Heavy Flavour Benchmarks of ILD

A. Irles, V. Lohezic, Y. Okugawa, R. Pöschl, F. Richard, H. Yamamoto, R. Yonamine

Abstract

An overview of the performance of the ILD detector in its version Large and Small as relevant for the IDR is given

1. Introduction

Heavy quarks may be messengers of new physics of primary importance. High precision e^+e^- collisions with polarised beams around the TeV scale are ideally suited to detect new physics effects [1, 2]. The detection of the onset of new physics require however a superb detector performance in terms of flavor tagging including the event by event determination of the charge of the final state jets. The charge determination happens mainly by a combination of the determination of the summed charge of tracks pointing to a secondary vertex or by the identification of the charge of a final state Kaon. This is turn requires a successful particle identification by the detector. Therefore processes with heavy quark final states, i.e. $e^+e^- \to b\bar{b}$ and $e^+e^- \to t\bar{t}$ are highly relevant for the benchmarking of the detector performance. In short one can test the following detector capacities.

- Track finding efficiency
- Stringent test of (secondary) vertexing
- Particle ID
- In case of $e^+e^- \to t\bar{t}$ leptonic and semi-leptonic decays of the top-quark pair provide an important additional handle for the accurate measurement of the final state. The analysis presented in this note focuses on the semi-leptonic decay mode of the top-quark pair.

The analyses presented in this note start out from the PhD thesis of Sviatoslav Bilokin that are based on the DBD samples and software versions [3]. This work has in part been published in Ref [2]. The analyses are ported to the large, IDR-L, and small, IDR-S, detector models, respectively, and are carried out with the software version that is relevant for the IDR of ILD. For the process $e^+e^- \to b\bar{b}$ an analysis at $\sqrt{s} = 500\,\text{GeV}$ is presented instead of $\sqrt{s} = 250\,\text{GeV}$ as in Ref. [2]. The results here benefit from a refined analysis strategy for the ILD paper that is under review in ILD.

2. Methods, tools and Monte Carlo samples

For the event reconstruction we use the `ILCSoft` version `v02-00-02` We use the following methods

- 'Core tools'
  - We use the `ValenciaVertex` jet algorithm implemented in `LCFIPlus` that provides the rejection of $\gamma\gamma$ background. In this algorithm the distance between two objects is calculated as

$$d_{ij} = 2\min(E_i^{2\beta}, E_j^{2\beta})(1 - \cos\theta_{ij})/R^2 \quad (1)$$

The distance of a particle i to the beam is calculated according to.

$$d_{iB} = E^{2\beta} \sin^{2\gamma} \theta_{iB} \tag{2}$$

The jet algorithm is run with the following settings: $\alpha = \beta = \gamma = 1$, $R = 1.4$

- We use the `LeptonFinder` in case of semi-leptonic $e^+e^- \to t\bar{t}$ events
- For the vertex finding we use the `LCFIPlus` in a private version maintained by Ryo. This version will soon be implemented into the official ILCsoft package.

- Tools developed for the study
  - The `VertexRestorer` Processor identifies tracks that have not been associated to secondary vertices from B-Meson decays but belongs to this decay according to the Monte Carlo Truth information. It then recovers the 'lost' tracks by means of the impact parameters d_0 (transversal) and z_0 (longitundinal). In this present note the recovery uses only the impact parameter d_0 since the algorithms needs to be adapted for the vertex smearing present in the simulation for the IDR.
  - The `ParticleTagger` Processor identifies the Kaons by means of the dE/dx measured in the TPC of ILD. It selects a strip in the dE/dx-momentum plane with a high kaon concentration. The efficiency and the purity of the Kaon selection vary as a function of the width of this strip.
  - The `QQbarAnalysis` Processor calculates the jet charge and the polar angle of the bottom and top quark pair, respectively. It contains separate methods for the bottom and top quark pair analysis.
  - The `TrashRecoProcessor` enables comparisons between reconstructed and generated quantities.
  - The described tools are available under https://github.com/QQbarAnalysis. This repository contains also a set of macros necessary for the final steps of the analysis.

- Quark charge measurement and corrections for miscalculations
  - Probabilities on double charge measurements for $t\bar{t}$ and $b\bar{b}$ has been examined.
  - Calculations scheme is shown below.

$$\left.\begin{aligned} N_{acc} &= Np^2 + Nq^2 \\ N_{rej} &= 2Npq \\ 1 &= p + q \end{aligned}\right\} \quad N_{corr} = N_{acc} \cdot \frac{p^2}{p^2 + q^2} \tag{3}$$

  - where N is total number of events, N_{acc} and N_{rej} are number of events that were accepted and rejected, respectively. The p and q values represent the probabilities for a correct or an incorrect reconstruction of the b quark charge, respectively. Solving this equation allows to correct for migrations caused by imperfect reconstruction or $B^0 - \bar{B}^0$ oscillations in the resulting polar angle spectrum.
  - the correction has been applied to the $b\bar{b}$ studies but not (yet) for $t\bar{t}$. For the latter the selection scheme in $t\bar{t}$ is more involved rendering its application less straight forward since e.g. the b-quarks are not necessarily back-to-back.

2.1. Monte Carlo samples and Event processing

For this benchmark study only processes with *left-handed* electron beam polarisation and *right-handed* positron beam polarisation, i.e. $\mathcal{P}_{e^-}, \mathcal{P}_{e^+} = \mp 1$, have been studied so far. The final states resulting from this configuration are more demanding for the detector performance in terms of the control of migration effects. In both cases the samples available for small and large detectors are available and comparisons will be presented where appropriate.

In case of the top-quark study we have analysed samples for the beam polarisations $\mathcal{P}_{e^-}, \mathcal{P}_{e^+} = \pm 1, \mp 1$. In case of the bottom quark study we have studied only the configuration $\mathcal{P}_{e^-}, \mathcal{P}_{e^+} = \mp 1$ since only a restricted simulated sample was available and this study was initially just considered as a supporting study for the top-quark analysis.

More precisely the results presented in this note are based on the following samples:

- $e^+e^- \to t\bar{t}$:
  - $yyxye\nu$, $\mathcal{P}_{e^-}, \mathcal{P}_{e^+} = \mp 1$: https://ild.ngt.ndu.ac.jp/elog/opt-data/?GenProcessID=108670
    This sample contains the final state resulting from the $W \to e\nu$ decay.
  - $yyxye\nu$, $\mathcal{P}_{e^-}, \mathcal{P}_{e^+} = \pm 1$: https://ild.ngt.ndu.ac.jp/elog/opt-data/?GenProcessID=108670
    This sample contains the final state resulting from the $W \to e\nu$ decay.
  - $yyxyl\nu$, $\mathcal{P}_{e^-}, \mathcal{P}_{e^+} = \mp 1$: https://ild.ngt.ndu.ac.jp/elog/opt-data/?GenProcessID=108675.
    This sample contains the final state resulting from the $W \to \ell\nu$ decay with $\ell = \mu, \tau$. For the analysis presented here the final state with $\ell = \tau$ has been discarded.
  - $yyxyl\nu$, $\mathcal{P}_{e^-}, \mathcal{P}_{e^+} = \pm 1$: https://ild.ngt.ndu.ac.jp/elog/opt-data/?GenProcessID=108676.
    This sample contains the final state resulting from the $W \to \ell\nu$ decay with $\ell = \mu, \tau$. For the analysis presented here the final state with $\ell = \tau$ has been discarded.
- $e^+e^- \to b\bar{b}$: The $b\bar{b}$ events are extracted from a sample of simulated 2-quark events https://ild.ngt.ndu.ac.jp/elog/opt-data/?GenProcessID=250114. The generated cross section for these 2-quark events is 32470 fb and the total integrated luminosity is about 46 fb^{-1} The genuine $e^+e^- \to b\bar{b}$ at 250 GeV is about 4% of the total cross section yielding a total number of events of about 60000.

Note that the analysis of the $e^+_R e^-_L \to t\bar{t}$ came quite late in the study since it is generally considered that the (semi-leptonic) $e^+_L e^-_R \to t\bar{t}$ is the more challenging channel. Therefore the corresponding control plots in Secs. 3 and 5 are only given for this channel in this note.

3. Efficiencies and Control plots

Figure 1 demonstrates that the studies presented in this note test the detector performance for very different momenta of the final state b quark.

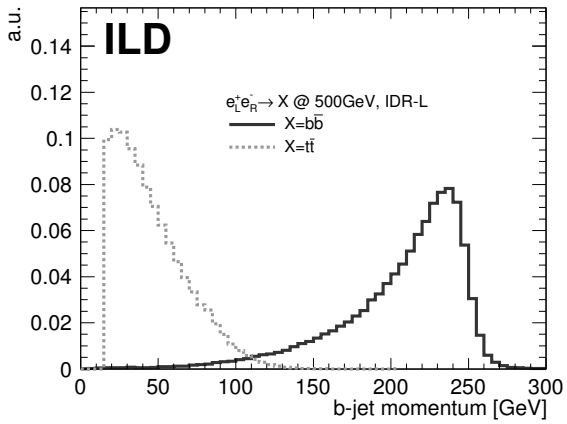

Figure 1: *Momentum of the b-jet with cheated identification for $e^+e^- \to b\bar{b}$ and $e^+e^- \to t\bar{t}$ processes.*

The Figs. 2 and 3 show the missed tracks before and after vertex recovery for the $e^+e^- \to b\bar{b}$ and $e^+e^- \to t\bar{t}$ analyses, respectively. Both figures suggest a systematic improvement in the assignment of secondary vertices.

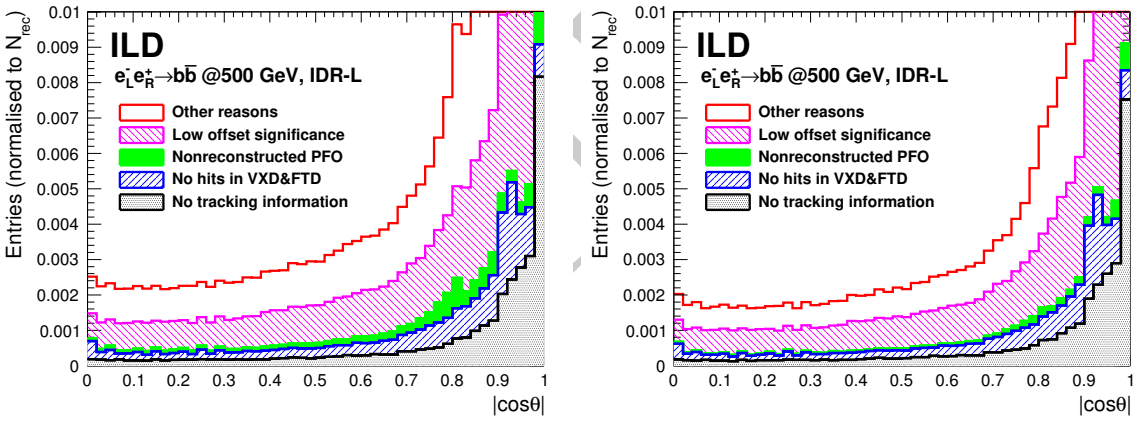

Figure 2: *Vertex recovery in case of the $e^+e^- \to b\bar{b}$ process.*

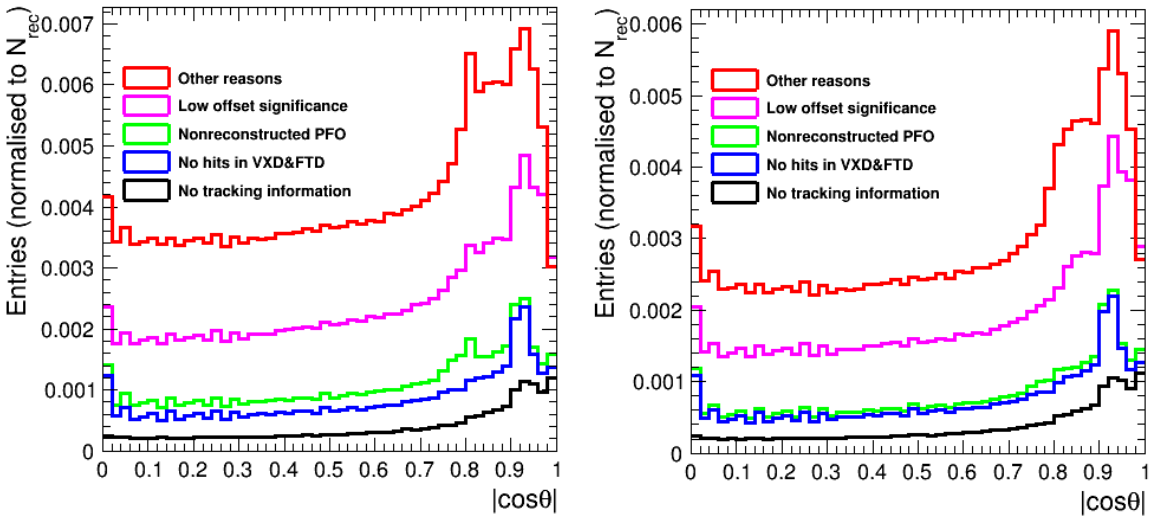

Figure 3: *Vertex recovery in case of the $e^+e^- \to t\bar{t}$ process.*

This improvement is quantified in Figs. 4 and 5 where the purity of the b-charge reconstruction is shown as a function of the $b-tag$ value, the reconstructed b-momentum $|p_{had}|$ the number of reconstructed tracks assigned to a secondary vertex N_{rec} and finally the polar angle of the b-hadron. here denoted as $|\cos\theta|$. The b-charge purity is defined as

$$p_b = N_{correct}/N_{jet,tot.} \tag{4}$$

with $N_{correct}$ being the number of b-jets with correctly reconstructed b-quark charge. This value normalised to the total number of b-jets $N_{b-jet,tot.}$ for which a charge assignment according to e.g. Table 2 can be made.

The improvemt is is larger for the process $e^+e^- \to t\bar{t}$ than for $e^+e^- \to b\bar{b}$. Qualitatively this is expected since as a consequence of the different b-jet momenta, see Fig. 1, also the tracks produced in the decay of the b-hadron are softer in case of top-pair production. In case of $e^+e^- \to t\bar{t}$ the improvement is 10% over a large range in $|\cos\theta|$ and mainly driven by three to five prong decays. Both results will further improve once the vertex recovery takes also the the impact parameter z_0 into account. All results shown so far in this section have been obtained for the large detector model. The conclusions for the small detector model are similar.

The lower right panels of Figs. 4 and 5 show a drop in purity for large values of $|\cos\theta|$. This is compatible with the drop in acceptance that is shown in Fig. 6 for the case $e^+e^- \to b\bar{b}$ as a function of the polar angle of the reconstructed b-jet $|\cos\theta_b|$. Within statistical errors the results are the same for the large and the small detector model. However, towards large values of $|\cos\theta_b|$ the large detector performs systematically better than the small detector.

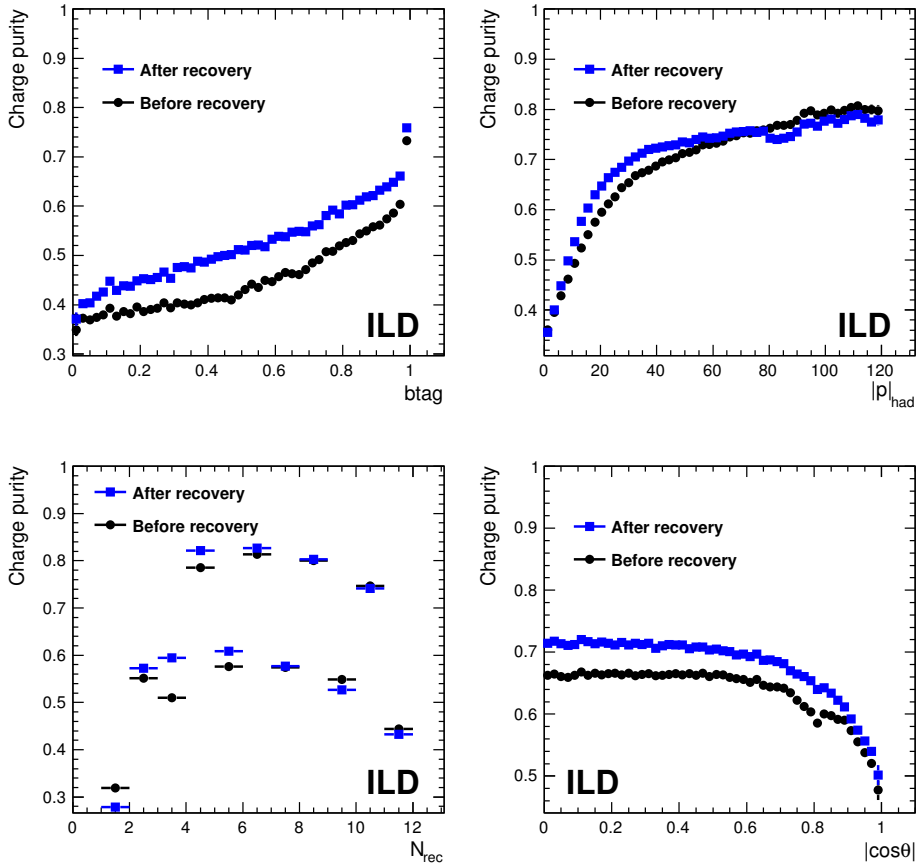

Figure 4: *Purity before and after vertex recovery in case of the $e^+e^- \to t\bar{t}$ process for different observables.*

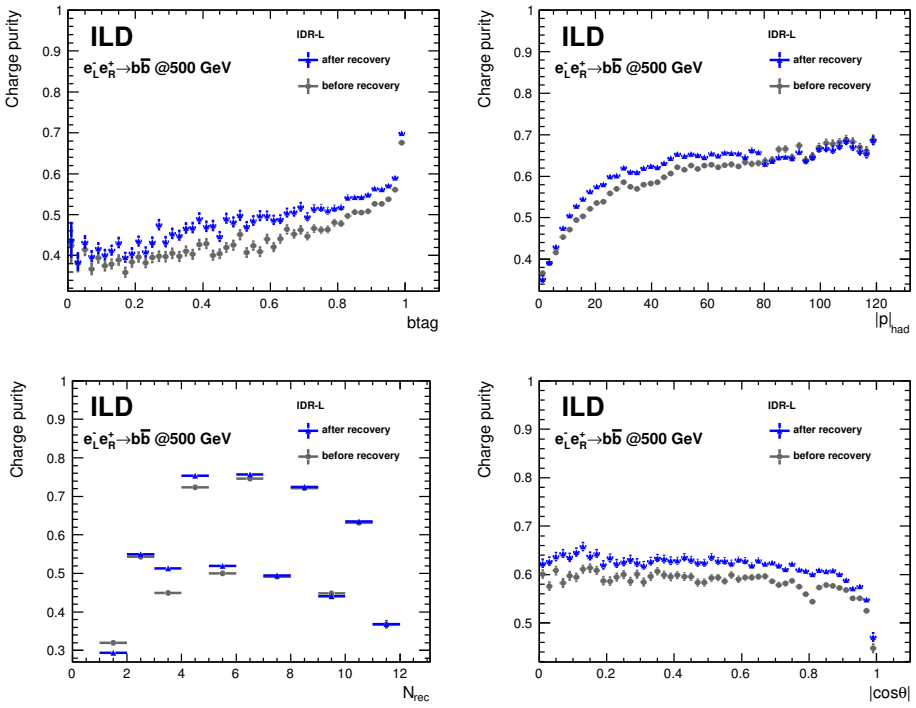

Figure 5: *Purity before and after vertex recovery in case of the $e^+e^- \to t\bar{t}$ process for different observables.*

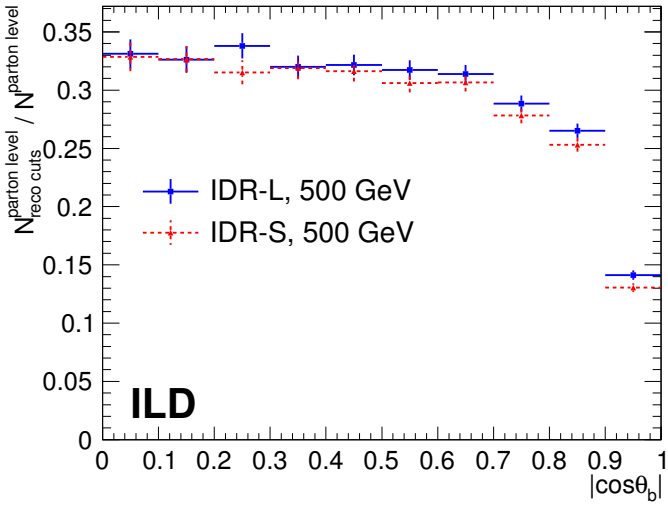

Figure 6: Detector acceptance distribution for b-tagged jets. Note the figure shows the acceptance after the full selection given in Tab. 1.

A component that distinguishes the ILD Detector from other proposals for e^+e^- colliders is the TPC as the central tracking system. Beside the precise momentum measurement the dE/dx measurement in the gaseous medium allows for a particle identification. Since around 80% of B-Mesons (neutral or charged) contain a charged Kaon among their decay products the particle ID can support greatly the

charge determination of the b-quark. The Fig. 7 displays the normalised dE/dx spectrum for different particles in different momentum ranges for the large and the small detector model. In both cases there is a clear separation of Kaons from pions. The latter are however much more abundant. There is only a small population of protons. Figure 8 shows the dE/dx spectra for the two processes under study. Finally the Fig. 9 shows the variation of the purity as as a function of the Kaon selection efficiency.

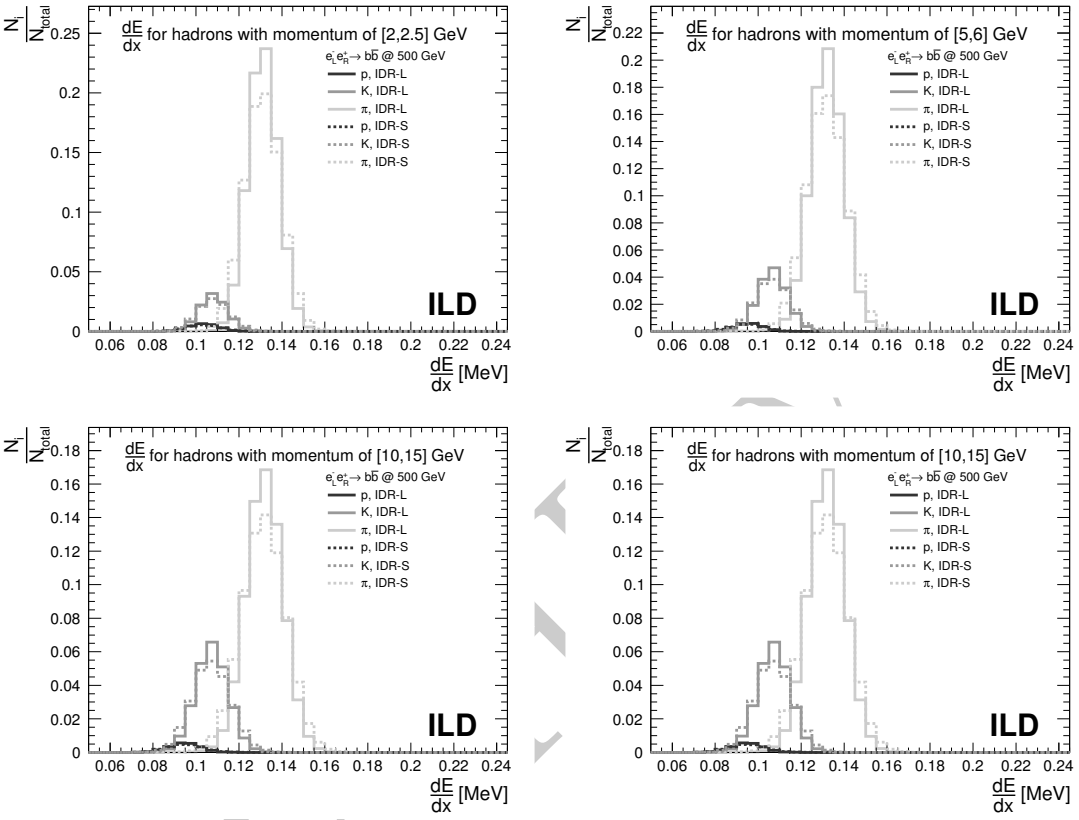

Figure 7: Projection of dE/dx for several momentum ranges. Comparison of hadron separation performance by different detector models in $b\bar{b}$ final states.

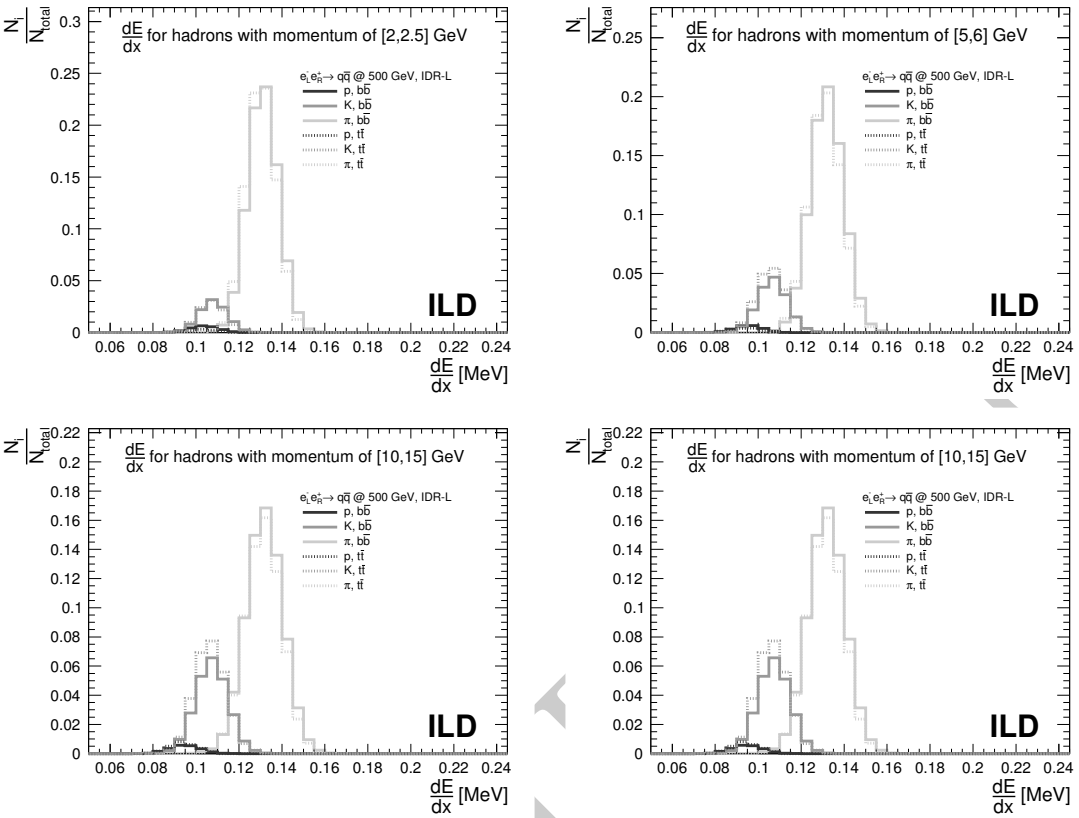

Figure 8: Projection of dE/dx for several momentum ranges. Comparison of hadron separation performance by the large model for different topologies.

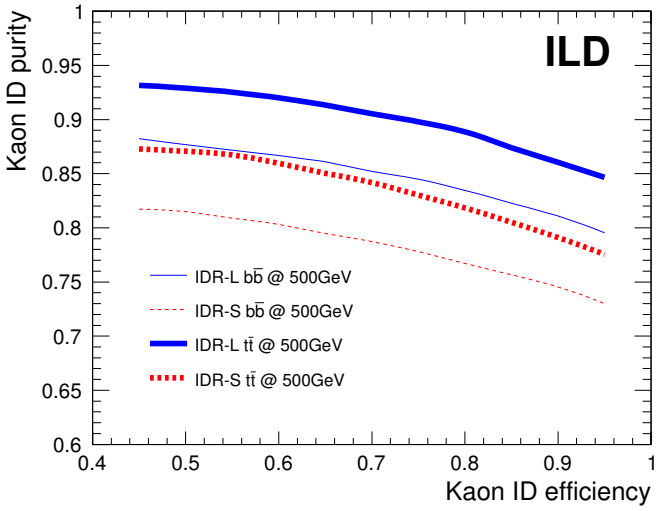

Figure 9: Purity of the Kaon selection as a function of the Kaon selection efficiency.

$e_L^- e_R^+ \to b\bar{b}$ at 500 GeV

	IDR-L			IDR-S		
	Signal	$B_{q\bar{q}}/S$	$B_{rad.Z}/S$	Signal	$B_{q\bar{q}}/S$	$B_{rad.Z}/S$
Full sample	100.0%	1800.5%	359.1%	100.0%	1800.6%	359.0%
$b_{tag}(jet_1) > 0.9$ and $b_{tag}(jet_2) > 0.2$	70.2%	2.3%	147.7%	69.9%	2.3%	149.0%
$m_{jet_1+jet_2} > 200GeV$	68.2%	1.4%	6.7%	67.8%	1.2%	6.7%
$E_{photon} < 100GeV$	64.8%	1.3%	1.7%	64.3%	1.2%	1.6%
double jet-charge measurement	28.9%	1.0%	1.0%	27.9%	0.9%	1.0%

Table 1: Selection efficiency and B/S rejection for some bkg sources

$e_L^- e_R^+ \to b\bar{b}$ at 500 GeV

	IDR-L	IDR-S
Vtx+Vtx	12.9%	12.8%
K+K	4.4%	4.0%
Vtx+K (diff. jets)	3.9%	3.7%
Vtx+K (same jet)	7.7%	7.4%

Table 2: Final selection efficiency, after double jet-charge measurement

4. Analysis details specific to the $e_L^- e_R^+ \to b\bar{b}$ analysis

Table 1 shows the selection efficiencies for the $e_L^- e_R^+ \to b\bar{b}$ analysis. The overall efficiency is with around 28% to 29% similar for both detector models. For the b-charge measurement opposite charges in opposite jets are required. The charges are either derived from the tracks pointing to the secondary vertex or from the Kaon charge or from a combination of both. The efficiencies for the different methods are given in Tab. 2. The purity of the different methods is shown in Fig. 10. In both cases there is no large difference between the two detector models although the large detector seem to perform slightly better for the double Kaon method.

5. Analysis details specific to the $e^+e^- \to t\bar{t}$ analysis

Figure 11 shows in the left panel the energy distribution of the isolated lepton in the laboratory frame. The distribution features a maximum at around 30 GeV and a tail towards higher energies. The right panel shows the polar angle spectrum of the isolated lepton. The distribution decreases slightly with a sharp drop at the acceptance limit of the detector. The distribution reveals also acceptance drops at $\cos\theta_\ell = 0$ and $\cos\theta_\ell = 0.8$ that correspond to the position of the TPC anode plate and the barrel-endcap transition region, respectively.

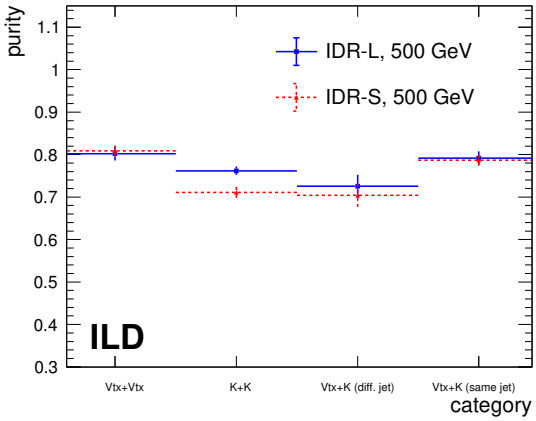

Figure 10: Purity of the different methods

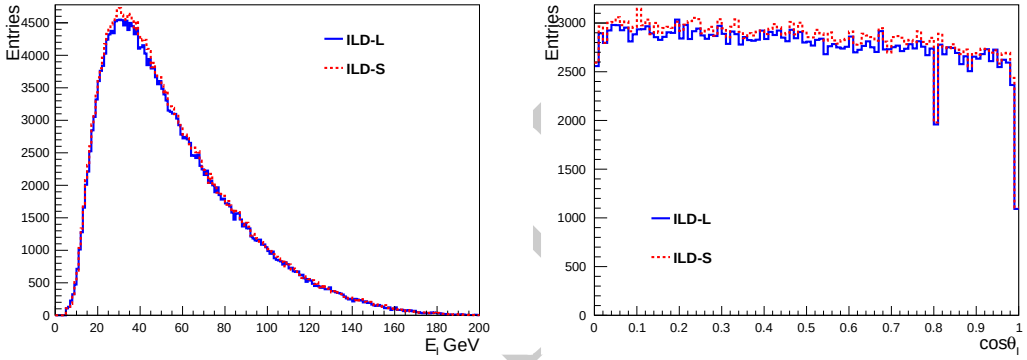

Figure 11: *Left: Energy of the isolated lepton in* $e_L^+ + e_R^- \to t\bar{t}$. *Right: Polar angle distribution of the isolated lepton in* $e_L^+ e_R^- \to t\bar{t}$.

For completeness Fig, 12 shows the mass distribution of the hadronic W and the hadronic top quark.

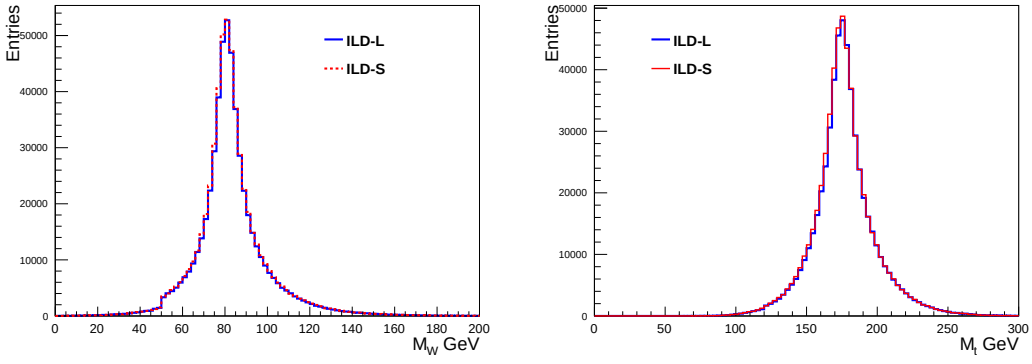

Figure 12: *Left: Mass distribution of the hadronic* W *in* $e_L^+ + e_R^- \to t\bar{t}$. *Right: Mass distribution of the hadronic top in* $e_L^+ e_R^- \to t\bar{t}$.

Tables 3 and 4 give the efficiencies after each cut applied for the selection of $t\bar{t}$ events.

$e^-_L e^+_R \to t\bar{t}$ at 500 GeV

	IDR-L	IDR-S
Isolated Lepton	92.1%	92.1%
$btag_1 > 0.8$ or $btag_2 > 0.3$	81.2%	81.1%
Thrust < 0.9	81.2%	81.1%
Hadronic mass	78.2%	78.2%
Reconstructed m_W and m_t	73.4%	73.4%

Table 3: Event selection efficiencies after each preselection criteria presented. Note that this does not concerns any background effects.

$e^-_R e^+_L \to t\bar{t}$ at 500 GeV

	IDR-L	IDR-S
Isolated Lepton	94.1%	94.0%
$btag_1 > 0.8$ or $btag_2 > 0.3$	84.9%	84.8%
Thrust < 0.9	84.9%	84.8%
Hadronic mass	82.2%	82.3%
Reconstructed m_W and m_t	77.6%	77.5%

Table 4: See Tab. 3 for details.

Figure 13 shows the fraction of accepted events, see Eq. 2 for different methods used to distinguish the top from the anti-top. The methods are the same as those given in Tab. 2. The semi-leptonic decay of the top quark gives an additional powerful information for the event reconstruction giving rise to the additional variable L_{cut}, which means the charge of the isolated lepton plus a cut on the event quality $\chi 2 < 15$ that is motivated in Ref. [1].

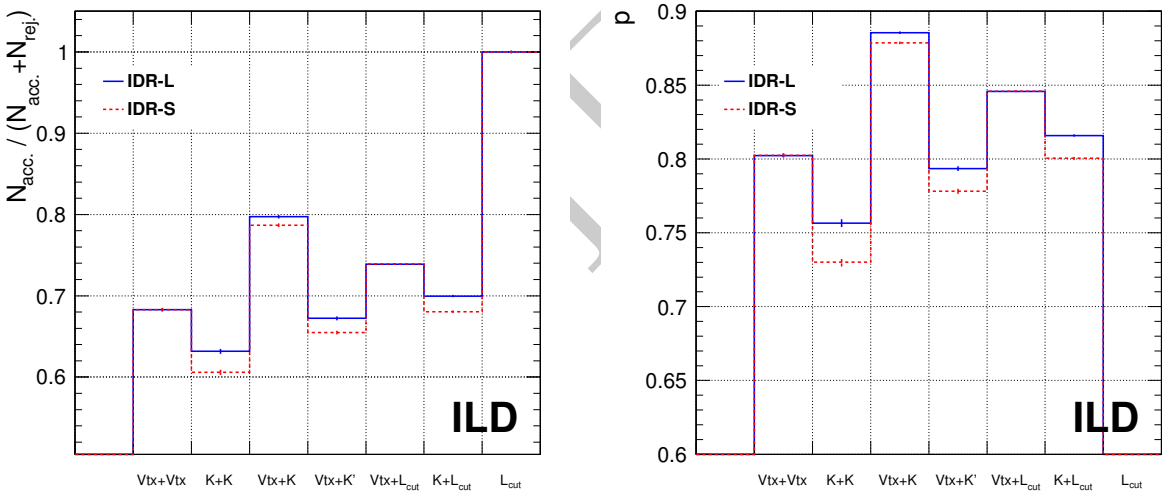

Figure 13: Calculated probability plots for $t\bar{t}$ events. Left: The result of $N_{acc.}/(N_{acc.} + N_{rej.})$. Right: Purities for different charge configurations. THE LEFT PART OF THIS FIGURE STILL NEEDS REVISION.

6. Results

Figure 14 shows the polar angle spectrum after the application of Eq. 2 for the $e^-_L e^+_R \to b\bar{b}$. Large and small detector agree within statistical uncertainties. It seems however that there is larger migration for the small detector.

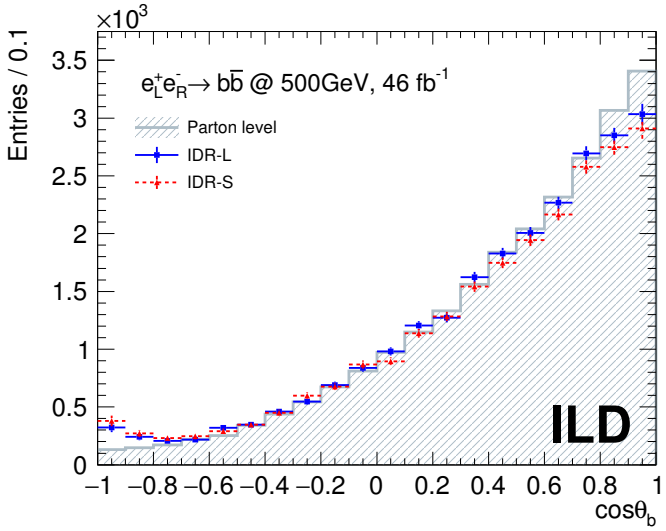

Figure 14

The left part of Fig. 15 shows the polar angle distribution of $t\bar{t}$ of the generated and reconstructed data for the large and the small detector models. For this all methods introduced in Fig. 13 have been applied. In addition events have been selected for which the momentum of the reconstructed B-hadron is greater than 15 GeV whenever the result of the vertex charge is used for a jet and the sum of the Lorentz γ of the top-quark pair is required to be greater than 2.4. The red dotted line shows the fitted result of the reconstructed events. The right part shows the polar angle distribution of the underlying b-quark for the same set of cuts.

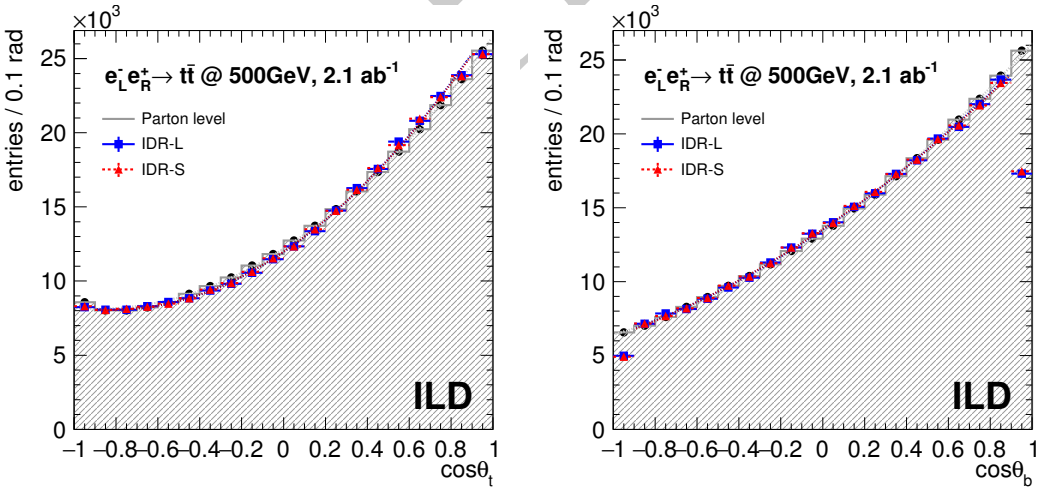

Figure 15: *Results for $e_L^- e_R^+ \to t\bar{t}$ Left: Polar angle distribution for top quark. Right: Polar angle distribution for the b-quark that is issue of the top-quark decay. The distributions for IDR-S is normalised to the one for IDR-L so that both histograms will be on the same level.*

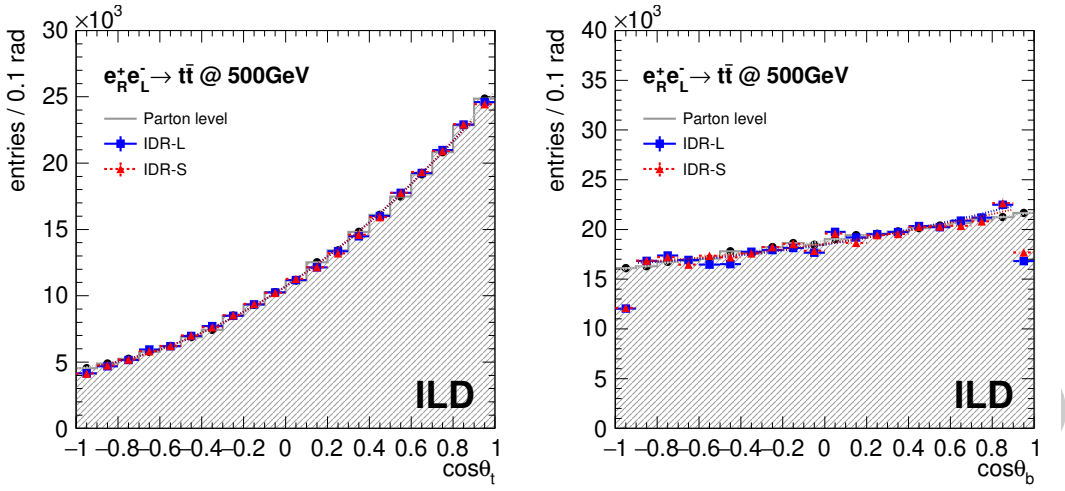

Figure 16: *Same as Fig. 15* $e^-_R e^+_L \to t\bar{t}$.

The left part of figure 17 shows the polar angle spectrum for the case $e^-_R e^+_L \to t\bar{t}$. For this the events remaining after the cuts in Table 4 are only subject to a further cut on the sum of the Lorentz γ of the top-quark pair of 2.4 as in the case of the $e^-_L e^+_R \to t\bar{t}$ channel. The generated spectrum can be reconstructed very precisely. The right hand part of Fig. 17 shows the polar angle spectrum of the underlying b-quark. Here only events with consistent vertex-charge measurements have been included. The polar angle of the b-quark can also in this case be very well reconstructed. However, the efficiency drops to 10%. The inclusion of the other methods is subject to further studies. Preliminary results show that taking into account the isolated lepton "swamps" the polar angle spectrum with events in which the b-quark direction is not constrained. One reason is certainly that in the case of $e^-_R e^+_L \to t\bar{t}$ the b-quark is on average softer than in the case of $e^-_L e^+_R \to t\bar{t}$.

Comparing the spectra of the underlying b-quarks demonstrate more clearly than the actual top-polar angle spectra the different polarisation of the top quarks projected out by the flight direction of the b-quark. In case of $e^-_L e^+_R \to t\bar{t}$ the final state is enriched with left-handed top-quarks. In this case the b-quark is preferably emitted in the direction of the top-quark. Therefore the two polar angle spectrum in Fig. 15 looks similar to each other. In case of $e^-_L e^+_R \to t\bar{t}$ In case of $e^-_R e^+_L \to t\bar{t}$ the final state is enriched with right-handed top-quarks. In this case the b-quark is preferable emitted opposite to the direction of the top-quark. The polar angle of the b-quark is a consequence of the Jacobian peak in the vicinity of $\cos\theta_{Wb} = 0$, with $\cos\theta_{Wb}$ being the opening angle between the b-quark and the W-boson, generated by the boost of the back-to-back configuration in the centre-of-mass frame of the decaying top into the laboratory frame.

Table 5 lists the overall selection efficiencies and the generated and reconstructed value of the forward-backward asymmetry $A^t_{FB,reco}$ as an estimator for the quality of the reconstruction.

	$e^-_L e^+_R \to t\bar{t}$		$e^-_R e^+_L \to t\bar{t}$	
	IDR-L	IDR-S	IDR-L	IDR-S
$A^t_{FB,gen}$	0.329		0.430	
$A^t_{FB,reco}$	0.342	0.340	0.430	0.430
$\varepsilon_{A^t_{FB,reco}}$	0.306	0.305	0.641	0.641

Table 5: *Selection efficiencies and resulting* $A^t_{FB,reco}$ *for both beam polarisations and the two detector models under study.*

So far the results have been presented for full beam polarisation. Using the known formula [4]

$$\sigma_{\mathcal{P}_{e^-},\mathcal{P}_{e^+}} = \frac{1}{4}\left[(1-\mathcal{P}_{e^-}\mathcal{P}_{e^+})(\sigma_{-,+}+\sigma_{+,-}) + (\mathcal{P}_{e^-}-\mathcal{P}_{e^+})(\sigma_{+,-}-\sigma_{-,+})\right] , \tag{5}$$

with $\sigma_{-,+}$ and $\sigma_{+,-}$ being the fully polarised cross-sections, the results can be extrapolated to the realistic beam polarisations of $\mathcal{P}_{e^-},\mathcal{P}_{e^+} = \mp 0.8, \pm 0.3$. The resulting Born level cross sections are $1070\,\mathrm{fb}^{-1}$ in case of $\mathcal{P}_{e^-},\mathcal{P}_{e^+} = -0.8, +0.3$ and $519\,\mathrm{fb}^{-1}$ in case of $\mathcal{P}_{e^-},\mathcal{P}_{e^+} = +0.8, -0.3$. The resulting statistical errors for an integrated luminosity of $\mathcal{L} = 1600\,\mathrm{fb}^{-1}$ at each of the two polarisation settings are given in Table 6.

	$\mathcal{P}_{e^-},\mathcal{P}_{e^+}$	$(\delta\sigma/\sigma)_{stat.}$ [%]	$(\delta A^t_{FB}/A^t_{FB})_{stat.}$ [%]
IDR-L	$-0.8,+0.3$	0.17	0.7
	$+0.8,-0.3$	0.25	0.53
IDR-S	$-0.8,+0.3$	0.17	0.7
	$+0.8,-0.3$	0.25	0.53

Table 6: *Statistical precisions expected for the cross sections and A^t_{FB} for the case $\mathcal{P}_{e^-},\mathcal{P}_{e^+} = -0.8,+0.3$ and the two detector models under study.*

For both, the cross section and the forward backward asymmetry it can be expected that even at full luminosity the statistical error has to be taken into account. However, the systematic errors need to be carefully estimated. For the present analysis it would have to be checked how much the sample is contaminated by events for which the semi-leptonic decay yields τ-leptons or the τ-leptons are taken into account as in [1]. The contamination by fully hadronic $t\bar{t}$ events can be expected to be small.

To put the results into context, the precisions on the cross-sections and the forward-backward asymmetries are translated into precisions on electromagnetic form factors of the top quark. Figure 17 shows the precisions at the $1\,\sigma$ level expected at ILC500. The precisions are compared with those expected after the full HL-LHC running and estimations produced for FCC-ee [5] at the same confidence level. For ILC500, the two sets F_1 and F_2 have been extracted separately but within each set the uncertainties have been extracted simultaneously. The projections for HL-LHC are derived from the *individual* constraints of EFT Wilson coefficients presented in Tab. C2.3 of Ref. [6] (the most favorable scenario for HL-LHC). These figures demonstrate clearly the superiority of a linear e^+e^- collider with polarised beams operated at an adequate centre-of-mass energy.

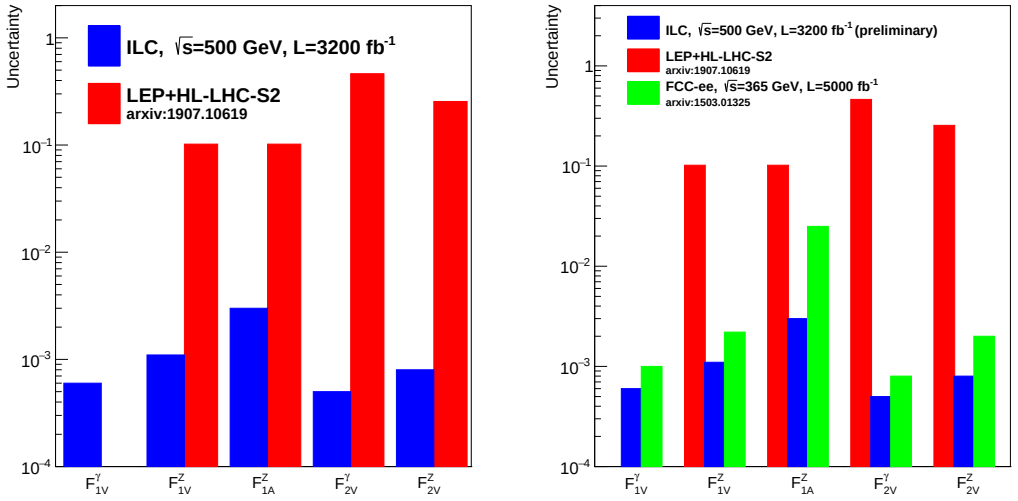

Figure 17: *Precisions the on electromagnetic form factors expected after ILC500 compared with those expected after the full HL-LHC running and an estimation for FCC-ee after* 5000 fb^{-1}. *See text for further details.*

7. Summary

The analysis shows that both, the large and the small detector model are capable to provide a high precision measurement of the cross-section and the polar angle spectrum of semi-leptonic $t\bar{t}$ events. The statistical precision on the cross section and the forward backward asymmetries are compatible with the results found in [1]. For the first time the underlying polar angle spectrum of the b-quark issue of the top quark decay is presented. This spectrum reveals more clearly the acceptance drop towards large polar angles. Still the polar angle of the b-quark can be reconstructed accurately within $\cos\theta < 0.8$ in case of $e^-_L e^+_R \to t\bar{t}$. The generated and reconstructed spectra are tilted for the case $e^-_R e^+_L \to t\bar{t}$. Here further work is clearly needed. Future studies should include the application of Eq. 2 for the $t\bar{t}$ case and a revision of the vertex recovery (list not exhaustive). However, both cases allow still for the perspective that in the future the fully hadronic final state can be taken into account for the analysis. It is likely that this will increase yet more the precision on the form factors shown in Fig. 17.

The study of the $t\bar{t}$ production has been accompanied by the second benchmark study $e^+e^- \to b\bar{b}$. Since only 46 fb^{-1} are available for this channel it should be rather considered as an auxiliary study. However, it is shown that the polar angle spectrum can be very well reconstructed even for the hard b-jets and that migrations can be controlled at a satisfactory level. It is therefore justified to conclude that ILD should be able to make precision measurements of this channel even at a centre-of-mass energy of 500 GeV. Although the results are similar for both the small and the large detector model, this analysis, more than the analysis of the $t\bar{t}$ process reveals a slight preference for the large model.

Also in the future all heavy quark studies should be carried out in close cooperation with each other. As can be seen from the present study there are many common issues between the studies. In the future emphasis will be put on systematic uncertainties given e.g. by hemisphere correlations. These studies may be more involved in case of $t\bar{t}$ since the heave quarks are in general not back-to-back.

Acknowledgements

References

[1] M. S. Amjad *et al.*, "A precise characterisation of the top quark electro-weak vertices at the ILC", *Eur. Phys. J.* **C75** (2015) no. 10, 512, IFIC-15-15, LAL-15-111, arXiv:1505.06020 [hep-ex].

[2] S. Bilokin, R. Pöschl, and F. Richard, "Measurement of b quark EW couplings at ILC", LAL-17-052, arXiv:1709.04289 [hep-ex].

[3] S. Bilokin, *Hadronic showers in a highly granular silicon-tungsten calorimeter and production of bottom and top quarks at the ILC*. Theses, Paris Saclay, July, 2017. https://tel.archives-ouvertes.fr/tel-01826535.

[4] G. Moortgat-Pick, T. Abe, G. Alexander, B. Ananthanarayan, A. Babich, *et al.*, "The Role of polarized positrons and electrons in revealing fundamental interactions at the linear collider", *Phys.Rept.* **460** (2008) 131–243, CERN-PH-TH-2005-036, DCPT-04-100, DESY-05-059, FERMILAB-PUB-05-060-T, IPPP-04-50, KEK-2005-16, PRL-TH-05-01, SHEP-05-03, SLAC-PUB-11087, arXiv:hep-ph/0507011 [hep-ph].

[5] P. Janot, "Top-quark electroweak couplings at the FCC-ee", *JHEP* **04** (2015) 182, arXiv:1503.01325 [hep-ph].

[6] G. Durieux, A. Irles, V. Miralles, A. Peñuelas, R. Pöschl, M. Perelló, and M. Vos, "The electro-weak couplings of the top and bottom quarks – global fit and future prospects", arXiv:1907.10619 [hep-ph].

Appendix

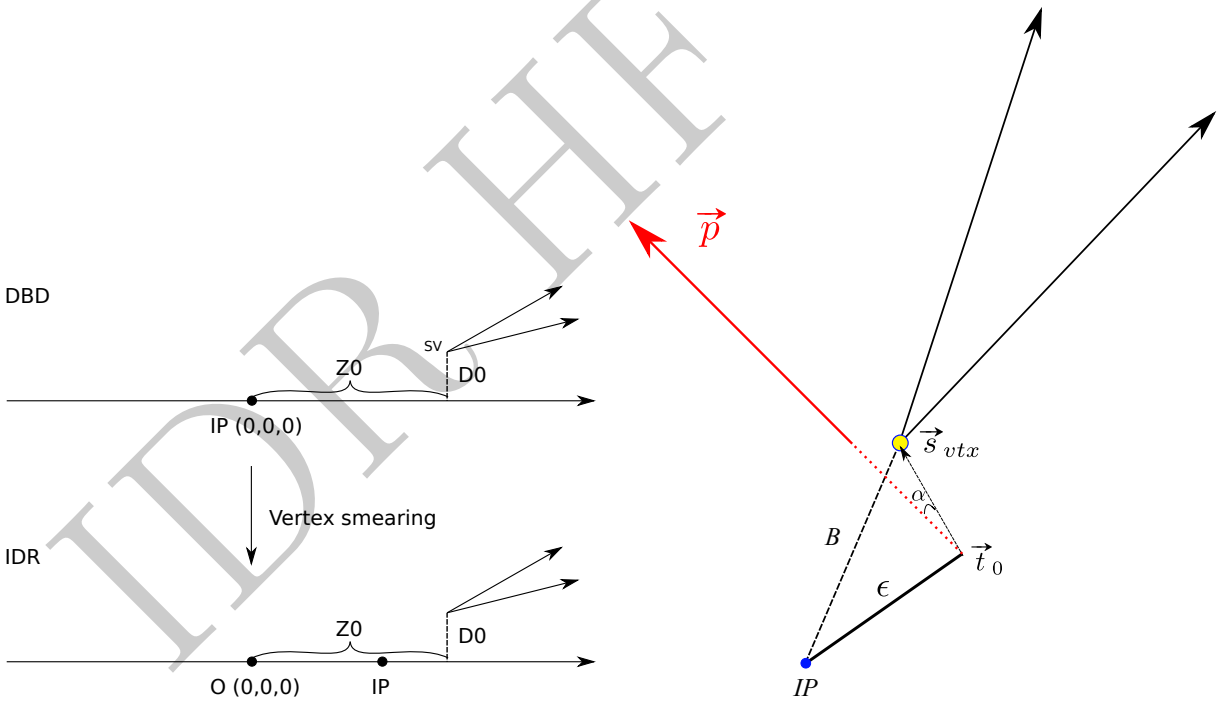

Figure 18: Left is